



## Article

# Study on Aeolian Sand-Box Backfill Geomechanical Characteristics and Overlying Strata Control Effects

Bo Zhao <sup>1,2</sup> , Zhiyi Zhang <sup>1,2,\*</sup>, Xiaoping Gong <sup>1,2</sup>, Wei Wang <sup>1,2</sup>, Xiaoyong Tong <sup>3</sup>, Hui Chen <sup>1,2</sup>, Weiming Guan <sup>1,2</sup> , Xin Li <sup>1,2</sup>, Shuo Feng <sup>1,2</sup>, Dezhi Yang <sup>4</sup>, Lubo Huang <sup>4</sup> and Yuhang Zhao <sup>1</sup>

<sup>1</sup> School of Geology and Mining Engineering, Xinjiang University, Urumqi 830046, China; zhaoxju@163.com (B.Z.); gxiaoping01@163.com (X.G.); wangweic104@163.com (W.W.); chenhui@xju.edu.cn (H.C.); gwmxju@xju.edu.cn (W.G.); lixinwaxj@xju.edu.cn (X.L.); fengshuo@xju.edu.cn (S.F.); zyh970126@163.com (Y.Z.)

<sup>2</sup> Collaborative Innovation Center of Green Mining and Ecological Restoration for Xinjiang Mineral Resources, Urumqi 830046, China

<sup>3</sup> The First Hydrology Engineering Geological Brigade of Xinjiang Bureau of Geology and Mineral Resources, Urumqi 830046, China; xiongershan@163.com

<sup>4</sup> No. 156 Coalfield Geological Exploration Team, Xinjiang Uygur Autonomous Region Coalfield Geological Bureau, Urumqi 830046, China; mhfd156@163.com (D.Y.); hlb328822@163.com (L.H.)

\* Correspondence: xjuzhiyi@163.com

**Abstract:** The aeolian sand-box backfilling method proves effective for environmentally friendly coal extraction in northwestern regions, including Xinjiang. This study investigated the geomechanical characteristics of aeolian sand-box backfill material and its control effects on overlying strata through indoor experiments, mechanical analysis, and numerical simulations. Uniaxial compression tests on models with varying mesh sizes, wire diameters, and dimensions revealed that larger mesh sizes and wire diameters increased the bearing capacity of the aeolian sand-box backfill material, while increasing dimensions had the opposite effect. A mechanical analysis of the metal mesh box deformation produced equations describing its restraining force. Subsequent experiments and simulations on models of different dimensions consistently demonstrated the material's mechanical properties, with stress-displacement curves closely aligned. 3DEC5.2 software simulations highlighted the effectiveness of aeolian sand-box backfill material in controlling displacement and stress variations in goaf areas. Notably, smaller-sized backfill material exhibited a more pronounced impact on controlling overlying strata displacement and stress development.

**Keywords:** aeolian sand-box backfill material; uniaxial compression test; numerical simulation; backfill mining



**Citation:** Zhao, B.; Zhang, Z.; Gong, X.; Wang, W.; Tong, X.; Chen, H.; Guan, W.; Li, X.; Feng, S.; Yang, D.; et al. Study on Aeolian Sand-Box Backfill Geomechanical Characteristics and Overlying Strata Control Effects. *Minerals* **2023**, *13*, 1556. <https://doi.org/10.3390/min13121556>

Academic Editor: Abbas Taheri

Received: 22 October 2023

Revised: 14 December 2023

Accepted: 15 December 2023

Published: 18 December 2023



**Copyright:** © 2023 by the authors. Licensee MDPI, Basel, Switzerland. This article is an open access article distributed under the terms and conditions of the Creative Commons Attribution (CC BY) license (<https://creativecommons.org/licenses/by/4.0/>).

## 1. Introduction

Aeolian sand, abundant on the surface in the desertified mining regions of Northwestern China, represents a valuable raw material. Box confinement is an effective method for utilizing aeolian sand in goaf backfilling. In coal-rich regions such as the Junggar Basin, Turpan-Hami Basin, and Tarim Basin in Xinjiang, the surface terrain is predominantly arid to semi-arid deserts or desolate areas. Water resources are scarce, and the ecological environment is exceptionally fragile [1–4]. Moreover, in Xinjiang, coal resources are predominantly characterized by shallow and thick coal seams. When utilizing the subsidence mining method in goaf areas, the disruption and displacement of overlying strata are more prominent in comparison to scenarios involving deeper coal seams and greater mining depths. Large-scale mining operations are likely to exert a considerable impact, resulting in damage to surface vegetation and underground water resources, posing a substantial threat to the delicate ecological balance in the region. [5–10]. Therefore, in the current situation where the public is increasingly concerned about the living environment and the country

strongly advocates ecological civilization construction, for arid and semi-arid desertified mining areas with extremely scarce water resources, solid filling materials are the most ideal choice.

Aeolian sand is a prevalent resource in desertified mining areas of Xinjiang, offering wide availability and cost-effectiveness. It emerges as an optimal choice for solid backfill material in the goaf areas of this region [11–14]. Nevertheless, its application as a dry fill material in the goaf encounters evident limitations. Aeolian sand, lacking cohesion, proves ineffective in supporting overlying strata during dry filling (Figure 1a). This significantly compromises the control effectiveness of the filling material on the roof strata. Recognizing the inadequacies of aeolian sand as a loose dry fill material for supporting overlying strata, this study proposes the use of aeolian sand-box backfill material, incorporating metal mesh boxes and aeolian sand for goaf reclamation. This waterless technology addresses the issue of aeolian sand's incapacity to support the roof strata during dry filling (Figure 1b).

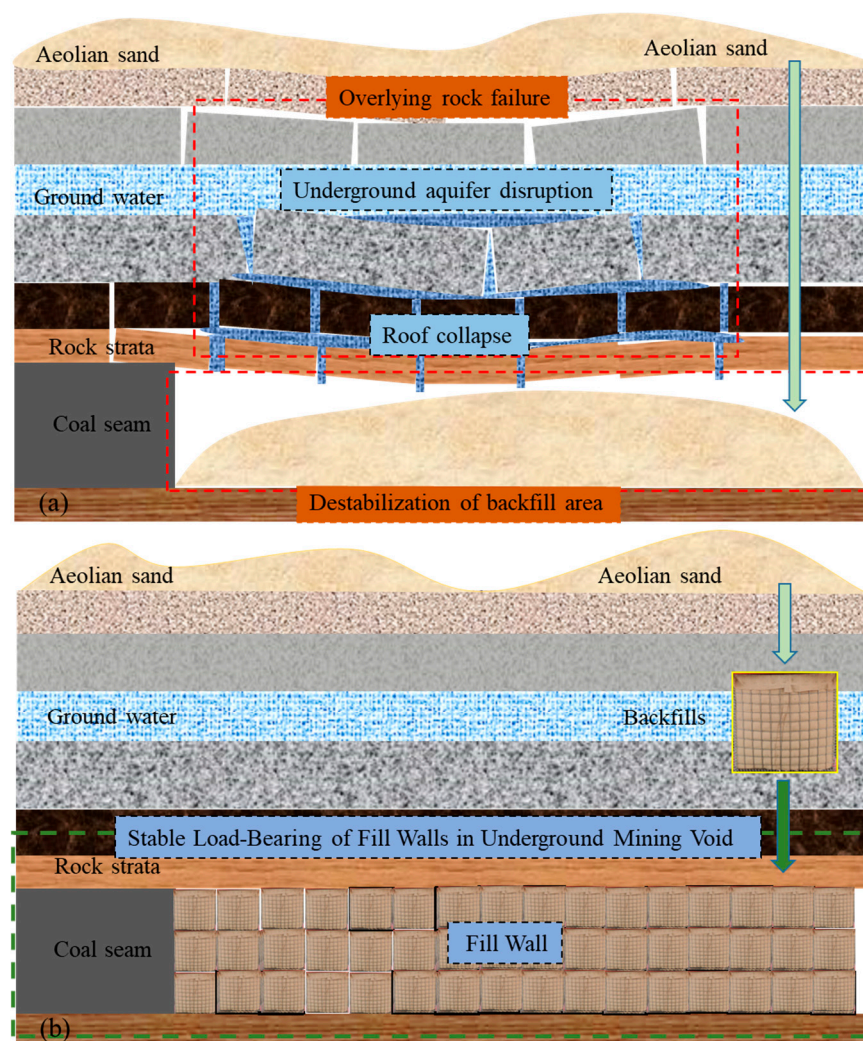


**Figure 1.** Schematic illustration of backfill mining (a) aeolian sand filling; (b) aeolian sand-box backfill material filling.

The stability of backfill material is crucial for effective subsidence control, with scholars providing key insights: Amin, Muhammad N [15], in mechanical experiments on coal gangue waste, analyzed the impact of lime and gypsum doses on the unconfined compressive strength of the coal gangue mixture. Gu Wei [16], combining lab experiments and numerical simulations, explored overlying strata movement patterns in gangue backfill mining. Results showed that narrower mining widths lead to less stress increase during

excavation and backfilling, enhancing backfill material stability. Mohammed Ashfaq [17] conducted a comprehensive review of factors influencing the mechanical properties of coal gangue and its geotechnical engineering applications. The study highlighted sustainable benefits in projects such as roadbeds and fill mining. Farshadi Anahita [18] stabilized windblown sand in Yazd, Iran, using glass fiber and nano-clay. The study indicated improved shear strength with the addition of these materials to aeolian sand. Maksimov Fedor [19] analyzed aeolian sand strength through numerical simulation and cyclic triaxial testing experiments, deriving a mechanical model applicable to soil damage. Huang Peng [20], considering the viscoelasticity of coal gangue, established a mechanical model for roof deformation. The model, using the lateral constraint compression method, provided accurate predictions for roof deflection and bending moments. Zhang Zhiyi [21] researched vibratory compaction of aeolian sand-box backfill material through lab experiments and PFC numerical simulations, revealing enhanced mutual compression under vibration. Zhang Zhiyi [22] studied the bearing strength of fill bricks composed mainly of aeolian sand and fly ash under different curing conditions. The conclusion highlighted the formation of dense needle-like calcium carbonate after carbonization and curing as the fundamental reason for increased bearing strength. Arias-Trujillo et al. [23–26] explored the mechanical properties of laterally constrained aeolian sand, finding that increased lateral constraint strength enhances load-bearing performance and provides stronger restraint against soil displacement.

In conclusion, both domestic and international scholars have predominantly regarded gangue and aeolian sand as supplementary materials in backfill research. However, there exists a notable gap in exploring the mechanical properties and overlying strata control effects of aeolian sand when used as a dry filling material. Addressing the challenges associated with low internal friction angles and limited support for overlying strata in aeolian sand, this study proposes the application of aeolian sand-box backfill material, incorporating metal mesh, geotextile, and aeolian sand. The research investigates its mechanical properties, mesh box stress, and overlying strata control effects, providing theoretical support and insights for the utilization of aeolian sand-box backfill in desertified mining areas in Xinjiang. This contribution aims to advance green mining practices in the region.

## 2. Materials and Methods

The study comprises four parts (Figure 2): the first assesses the mechanical performance of the aeolian sand-box backfill material model, examining the impact of wire diameter, mesh size, and dimensions on load-bearing capabilities; the second analyzes the mechanical deformation of the metal mesh in the aeolian sand-box backfill material, deriving a mechanical model for mesh box deformation using mechanical principles; the third conducts mechanical tests on the aeolian sand-box backfill material, establishing mechanical parameters for numerical simulations of backfill mining; in the fourth part, based on the above analyses, numerical simulations evaluate the backfilling effectiveness of the aeolian sand-box backfill material in the goaf area and analyze its overlying strata movement.

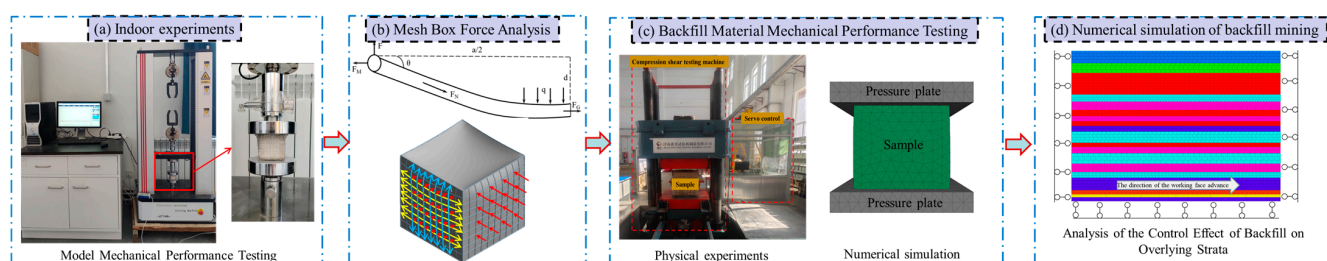


**Figure 2.** Research methods and procedures (a) model mechanical performance testing; (b) mesh box force analysis; (c) backfill material mechanical performance testing; (d) numerical simulation.

### 2.1. Model Fabrication

The metal mesh cage plays a crucial role in supporting the load within aeolian sand-box backfill structures. To explore, systematically and intuitively, the macroscopic influence of different mesh cage sizes, wire diameters, and mesh configurations (mesh counts) on the load-bearing performance of aeolian sand-box backfill structures, this study initially constructed physical models with variations in these three parameters. Due to a significant size difference between the aeolian sand-box backfill structure model and the prototype in Section 2.3.1, the specifications of mesh and geotextile fabric used in the model had to be smaller while maintaining consistent fabrication processes. Laboratory uniaxial compression tests were conducted to obtain curves for the backfill structure models.

In the experiments, the aeolian sand was collected from the surface of the Gashunhai No. 1 Coal Mine located on the edge of the Gurbantunggut Desert in Xinjiang. The metal mesh was made of factory-produced 304 low-carbon steel wire, and the fastening wire used was fine iron wire of 28-gauge. The geotextile material had a specification of 150 g/m<sup>2</sup>.

First, the metal mesh sheets were cut into square pieces of the required size. Next, fine iron wire was used to secure the bottom and the connections around the square mesh pieces. Then, geotextile was laid flat inside the mesh box, and aeolian sand was filled into the mesh box. Finally, uniaxial compression tests were conducted on the prepared aeolian sand-filled mesh box. The test process is illustrated in Figure 3.

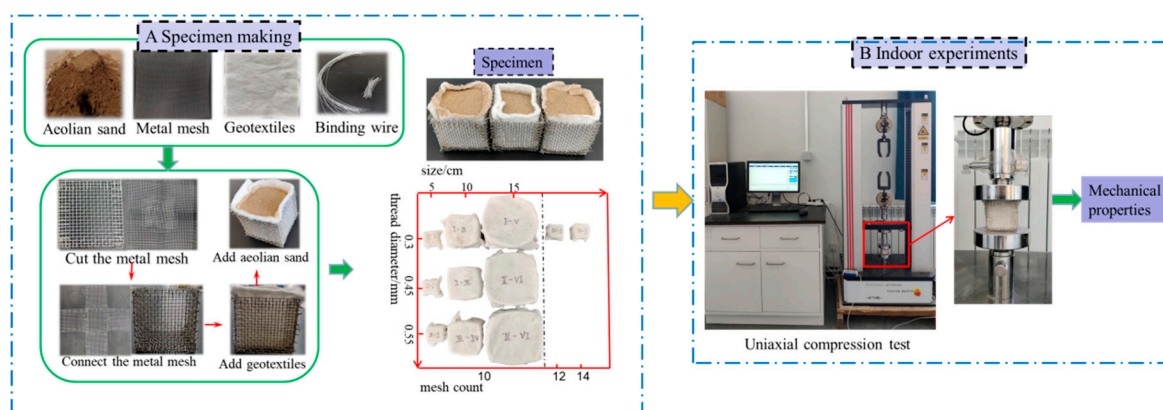


**Figure 3.** Process of fabrication and mechanical testing of similar materials.

In the experiments, a SANS CMT5305 brand hydraulic uniaxial compression machine (maximum test force: 300 kN; force accuracy:  $\pm 0.3\%$  or better) was used to conduct uniaxial compression tests on the aeolian sand-box backfill material (see Figure 3). The loading was displacement-controlled, with a loading rate of 1 mm/min. The test plan is detailed in Table 1.

**Table 1.** Experimental protocol for uniaxial compression.

Numbering	Mesh Count	Size/cm	Diameter/mm
1	10	5	0.3, 0.45, 0.55
2	10	10	0.3, 0.45, 0.55
3	10	15	0.3, 0.45, 0.55
4	12	5	0.3
5	14	5	0.3

### 2.2. Analysis of Mesh Box Stress and Deformation

The metal mesh box imparts lateral constraint forces to the aeolian sand. Investigating the stress distribution patterns of the wire mesh in the aeolian sand-box backfill material during stress and deformation is crucial for the enhanced design, application, and reinforcement of the material. In the mechanical model presented herein, the mesh box is

assumed to have equal dimensions in length, width, and height, with symmetrical metal mesh between the fastening wire connections on both sides of the mesh sheet. One-half of a single wire mesh is examined in the study. [27]. The stress analysis of the metal wire mesh is depicted in Figure 4.

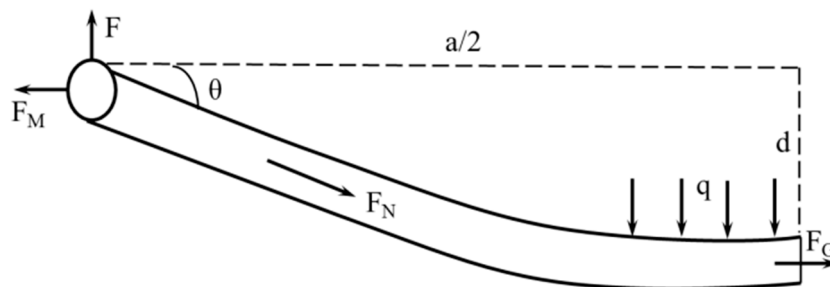


**Figure 4.** Force analysis diagram of the metal net cage.

The equilibrium equation is as follows:

$$F_G = F_N \cos \theta = F_M \quad (1)$$

$$qa/2 = F_N \sin \theta = F \quad (2)$$

In the above diagram,  $a$  represents the mesh box dimensions;  $F$  is the longitudinal wire tension;  $F_M$  is the tension at the connection point;  $F_N$  is the tension in the straight section of the wire mesh;  $F_G$  is the tension in the netted section of the metal wire mesh;  $q$  is the uniformly distributed load on the metal mesh; and  $d$  is the deflection.

The elongation of the steel wire after stress deformation [28]:

$$\Delta L = \frac{F_M}{k_1} + \frac{F_N}{k_2} + \frac{F_G}{k_3} \quad (3)$$

By simultaneously solving Equations (1)–(3), the tension at the metal mesh connection point is obtained:

$$F_M = \frac{1}{2} \frac{k_1 k_2 k_3 a \sqrt{1 + 4(d/a)^2} - 1}{k_2 k_3 + k_1 k_2 + k_1 k_3 \sqrt{1 + \tan^2 \theta}} \quad (4)$$

In the equation:  $k_1$  is the stiffness at the connection point;  $k_2$  is the stiffness of the curved section of the wire mesh; and  $k_3$  is the stiffness of the netted section of the wire mesh. By combining Equations (1) and (4), the tension in the straight section of the metal mesh is determined:

$$F_N = \frac{1}{2} \frac{1}{\cos \theta} \frac{k_1 k_2 k_3 a \sqrt{1 + 4(d/a)^2} - 1}{k_2 k_3 + k_1 k_2 + k_1 k_3 \sqrt{1 + \tan^2 \theta}} \quad (5)$$

Lateral constraint force of the metal mesh box:

$$M = 2 \left( \frac{a}{c} + 1 \right) \frac{k_1 k_2 k_3 a \tan \theta \sqrt{1 + 4(d/a)^2} - 1}{k_2 k_3 + k_1 k_2 + k_1 k_3 \sqrt{1 + \tan^2 \theta}} \quad (6)$$

In the equation:  $c$  is the aperture of the metal mesh.

From Equation (4), it is evident that  $F_M$  is a monotonically increasing function with respect to  $a$ , indicating that as the metal mesh box undergoes a specific load, the tension at the connection point rises with the augmentation of the mesh box dimensions. The connection point represents a vulnerable link in the mesh box, where localized stress concentration may occur. Therefore, during mesh box design, precautionary measures should be taken to mitigate the risk of connection point failure associated with an increase in dimensions.

From Equation (6), it is evident that the lateral constraint force of the metal mesh box is a decreasing function with respect to  $c$ . In other words, when the number of wire meshes per unit area inside the metal mesh remains constant, the greater the number of wire meshes, the more significant the lateral constraint force provided by the metal mesh box to the aeolian sand. A schematic illustration of the lateral constraint force provided by the metal mesh box to the aeolian sand is shown in Figure 5. The lateral constraint force of the metal mesh box is an increasing function with respect to the stiffness  $k_1$ , wire stiffness  $k_2$ ,  $k_3$ , and deformation angle. In other words, the lateral constraint force provided by the metal mesh box increases with the increase in stiffness and deformation angle. When the metal mesh box provides a certain lateral constraint force, the deformation angle decreases with the increase in stiffness. This implies that the deflection of the mesh box will also decrease. Therefore, in the fabrication of the mesh box, to save costs, one should not blindly increase the wire diameter or reduce the metal mesh aperture, which could lead to material wastage. Instead, the choice of wire diameter and aperture size can be determined based on the actual engineering requirements after establishing the allowable deformation range for the box.

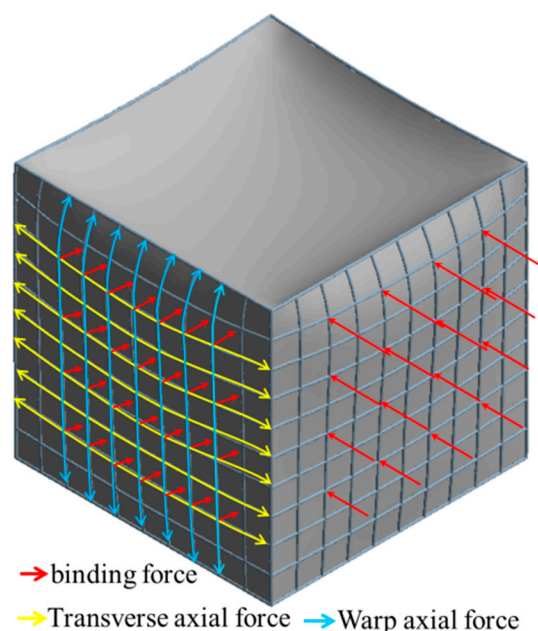


**Figure 5.** Schematic representation of lateral restraint forces on metal net cage.

### 2.3. Mechanical Performance Testing of Aeolian Sand-Box Backfill Material

To comprehend the mechanical properties of the aeolian sand-box backfill material, uniaxial compression tests were carried out on backfill materials of three different sizes, followed by a thorough analysis of their variations. Subsequently, the obtained mechanical parameters were employed in the 3DEC numerical simulation software to conduct backfill mining simulations.

#### 2.3.1. Laboratory Uniaxial Compression Tests

The aeolian sand-box backfill material consists of a metal mesh box, geotextile, and aeolian sand. The aeolian sand was collected from the surface of the Saji Hai No. 1 Coal Mine, located on the edge of the Gurbantünggüt Desert in Xinjiang. The geotextile had a specification of 320 g/m<sup>2</sup>. The wire material for the metal mesh box was low-carbon steel. The samples of aeolian sand-box backfill material were all in the form of cubes. The mesh box is shown in Figure 6, and the physical parameters are listed in Table 2. To investigate the mechanical properties of aeolian sand-box backfill material with different sizes, uniaxial loading tests were conducted on specimens with side lengths of 50 cm,

80 cm, and 100 cm. The loading was displacement-controlled using a YJW10000 computer-controlled electrohydraulic servo shearing test machine, with a loading rate of 10 mm/min, until the specimens and the loading was stopped. Finally, stress vertical displacement data were exported for analysis.

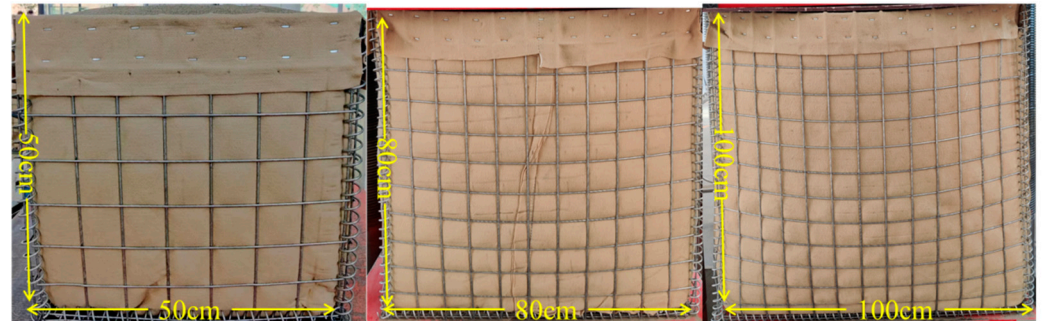


**Figure 6.** Aeolian sand-box backfill material samples.

**Table 2.** Physical parameters of aeolian sand-box backfill material.

Aperture/cm	Silk Diameter/mm	Size/cm
17.5	6	50, 80, 100

The experiments were conducted in the heavy-duty laboratory of the School of Architecture and Civil Engineering at Xinjiang University. The testing equipment used was the YJW-10000 computer-controlled electrohydraulic servo shearing test machine, as shown in Figure 7. This test platform can be used for tests with a model size of 1100 mm × 1100 mm and consists of upper and lower pressure plates, hydraulic apparatus, and a servo control room. It has a maximum loading capacity of 10,000 kN and can apply loads from the top and bottom to determine the specimen's bearing performance.

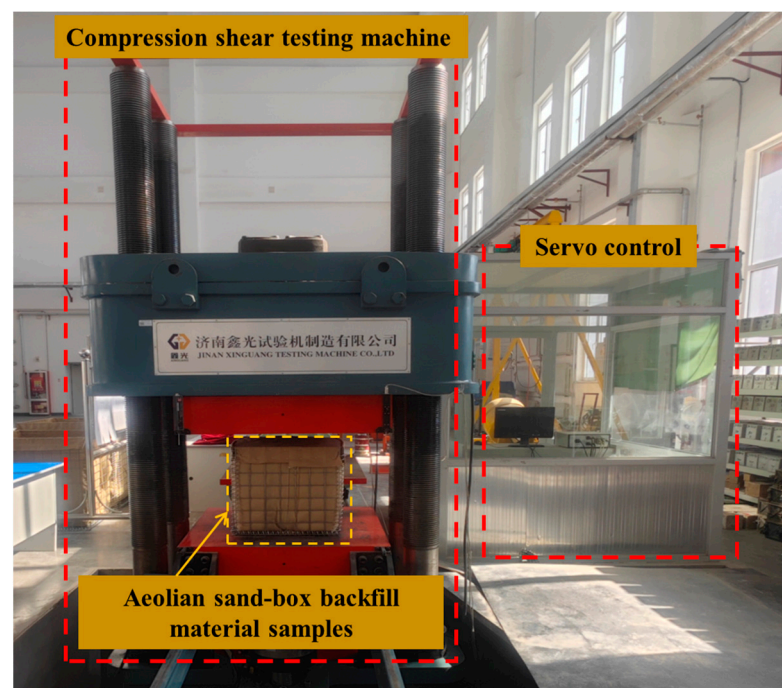


**Figure 7.** Shearing test machine.

### 2.3.2. Numerical Simulation of Uniaxial Compression Tests

Numerical simulation analysis of the force and deformation of the aeolian sand-box backfill structure was conducted using 3DEC simulation software, the numerical model is shown in Figure 8. The model consisted of upper and lower pressure plates and backfill material. In the first step, the ploy command was utilized to model the upper and lower pressure plates and the backfill material (50 cm, 80 cm, 100 cm). The upper and lower pressure plate models were defined as rigid, while the backfill material was characterized using the MohrCoulomb plasticity model. Subsequently, the edge command was employed to discretize the model with a grid size of 0.1. Following this, a loading condition was imposed on the upper and lower pressure plates at a velocity of 10 mm/min until failure occurred. The stress displacement curves resulting from the numerical simulation uniaxial compression test were then compared and analyzed in relation to those from the physical uniaxial compression test. Finally, the mechanical parameters derived from the numerical simulation were utilized in the 3DEC backfill mining simulation experiment.

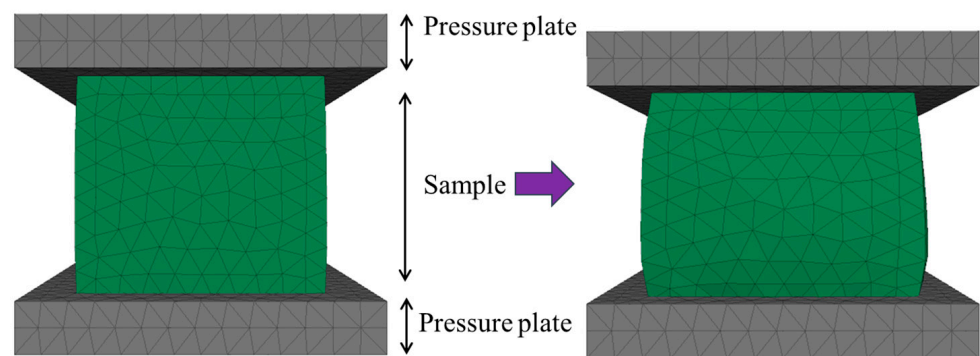


**Figure 8.** Numerical simulation of uniaxial compression test.

### 2.4. Backfill Mining Numerical Simulation

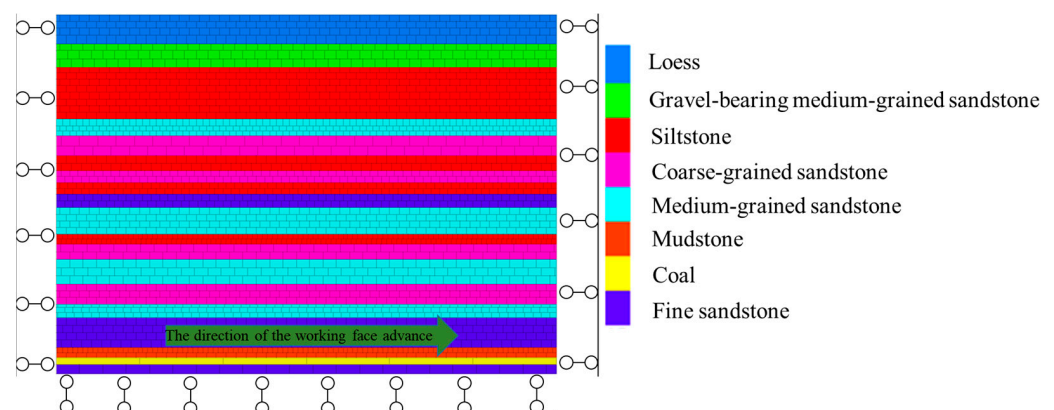
In this section, leveraging the prior investigation into the mechanical properties of backfill material, we implement the aeolian sand-box backfill material in the goaf and assess its impact on controlling the overlying strata. The findings will offer valuable insights into the utilization of aeolian sand-box backfill material in backfill mining projects.

#### Model Establishment

Modeling of rock layers and backfill material was performed using the 3DEC numerical simulation software. Initially, the entire model was defined using the PLOY command, and subsequently, the JEST command was utilized to establish the rock joints and contacts with the backfill material. The overall model had dimensions of 300 m in length, 4 m in width, a coal seam burial depth of 200 m, and a coal seam height of 4 m. Meshing was accomplished using the EDGE command, with a maximum grid size of 2 and a minimum of 0.2. The bottom and sides of the entire geological model were constrained. The MohrCoulomb constitutive model was applied to the rock layers and backfill material in the numerical simulation, with the joints modeled using the MohrCoulomb sliding model. Geological parameters for the numerical simulation were sourced from Wusu Four Trees Coal Limited Liability Company (Wusu, China). The study area is situated at the No. 8 well in Baiyanggou Town, 43 km southwest of Wusu City. The parameters for each geological layer are detailed in Table 3, and the model is depicted in Figure 9.

**Table 3.** Rock layer parameters in numerical simulation.

Number	Lithology	Depth/m	Density /kg/m <sup>3</sup>	Bulk Modulus /GPa	Shear Strength /GPa	Friction Angle/°	Tensile Strength /MPa
1	Loess	17	2200	0.05	0.03	25	0
2	Gravel-bearing medium-grained sandstone	14	2600	8.2	6.5	28	2.7
3	Siltstone	31	2620	5.8	4.7	35	2.4
4	Medium-grained sandstone	10	2650	12.8	9.2	36	3.5
5	Coarse-grained sandstone	12	2700	16.6	12.5	35	4.2
6	Siltstone	9	2620	5.8	4.7	35	2.4
7	Coarse-grained sandstone	7	2700	16.6	12.5	35	4.2
8	Siltstone	7	2620	5.8	4.7	35	2.4
9	Fine sandstone	8	2750	14.3	10.9	36	4.9
10	Medium-grained sandstone	16	2650	12.8	9.2	36	3.5
11	Siltstone	6	2620	5.8	4.7	35	2.4
12	Coarse-grained sandstone	9	2700	16.6	12.5	35	4.2
13	Medium-grained sandstone	15	2650	12.8	9.2	36	3.5
14	Coarse-grained sandstone	12	2700	16.6	12.5	35	4.2
15	Medium-grained sandstone	8	2650	12.8	9.2	36	3.5
16	Fine sandstone	18	2750	14.3	10.9	36	4.9
17	Mudstone	6	2580	4.6	3.7	22	2.1
18	Coal	4	1600	4.5	3.4	33	1.7
19	Fine sandstone	5.6	2750	14.3	10.9	36	4.9

**Figure 9.** Numerical simulation model.

On the basis of the previous model, coal seam mining with backfilling is simulated. In the first step, the ‘reset’ command is used to clear the displacement generated by self-weight stress in the model. To eliminate boundary effects caused by coal seam mining, 50 m coal pillars are left at both ends of the model. The ‘excavate’ command is used to simulate coal seam excavation, and the ‘fill’ command is employed for backfilling (200 m of filling). The simulation is conducted in two phases: (1) Simulation of coal seam excavation without backfilling the excavation is conducted in four steps, with each step involving the excavation of 50 m of coal. (2) Simulation of backfilling during mining: three different-sized aeolian sand-box backfill materials are used to backfill the mined-out area in four steps, with each step involving 50 m of excavation and 50 m of backfilling. The simulation setup is described in Table 4. The simulations include monitoring of displacements, stresses, and other factors. Specifically, vertical displacements of the roof above the coal seam are monitored. Monitoring points are spaced 25 m apart above the coal pillars and 20 m apart above the mined-out area. Vertical stress in the roof is monitored at points spaced 10 m apart. Finally, the development of fractures in the overlying rock strata at different advancement lengths is also monitored.

**Table 4.** Numerical simulation schemes.

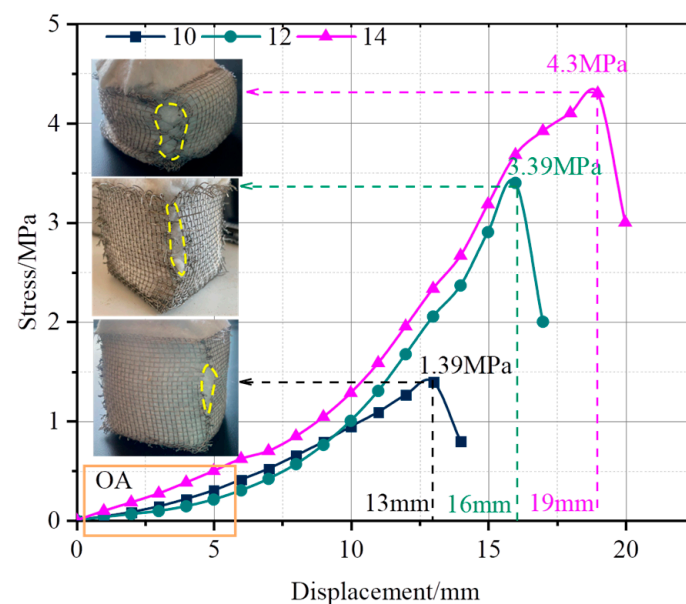
Mining Method	Backfill Size/cm	Advancing Distance/m
Sublevel caving Backfill mining	No 50, 80, 100	50, 100, 150, 200

### 3. Results

#### 3.1. Mechanical Properties of the Filling Material Model

##### 3.1.1. The Impact of Mesh Count on the Bearing Performance of the Filling Material

To investigate the influence of different mesh sizes on the load-bearing characteristics of the aeolian sand-filled box, this paper selected single-axis compression test data for the aeolian sand filling box with dimensions of 5 cm, mesh counts of 10, 12, and 14, and wire diameter of 0.3 mm for analysis. The result shows the vertical curves for the aeolian sand-filled boxes with different mesh counts, as depicted in Figure 10.

**Figure 10.** Influence of particle size on the mechanical properties of backfill material.

From Figure 10, it can be observed that the curve during the OA stage is nearly linear, indicating the compression and densification phase of the aeolian sand-filled box. This is because there are micro-pores between the aeolian sand particles, and under the influence of external forces, the particles redistribute, making the aeolian sand more compact. Beyond the OA stage, the aeolian sand inside the box becomes even more compact, and the pressure develops rapidly, resulting in an upward curvature in the curve. As the vertical load increases, the vertical displacement of the filling material increases, and at the same time, lateral deformation gradually increases. Since the connection area is a weak point in the box and can experience stress concentration locally, this ultimately leads to damage at the edge connections. This experimental phenomenon corroborates the macro-level conclusions mentioned in Section 2.2, specifically the findings from Equation (4). The observation that metal boxes with higher mesh numbers (14, 12, and 10) have better load-bearing performance is consistent with the conclusions derived from the mechanical formula in this paper (Equation (6)). It confirms that with a constant wire diameter, a higher number of wires per unit area inside the metal box leads to greater lateral constraint forces provided by the metal box for the windblown sand. As a result, the vertical load-bearing capacity of the windblown sand filling material improves.

### 3.1.2. The Impact of Wire Diameter on the Load-Bearing Performance of Backfill Material

In order to investigate the effects of different wire diameters on the mechanical properties of backfill material models, this study conducted uniaxial compression tests using wind-blown sand fill boxes with dimensions of 5 cm and mesh counts of 10. The wire diameters tested were 0.3 mm, 0.45 mm, and 0.55 mm. The analysis of the test data resulted in vertical curves for the mesh boxes, as depicted in Figure 11.

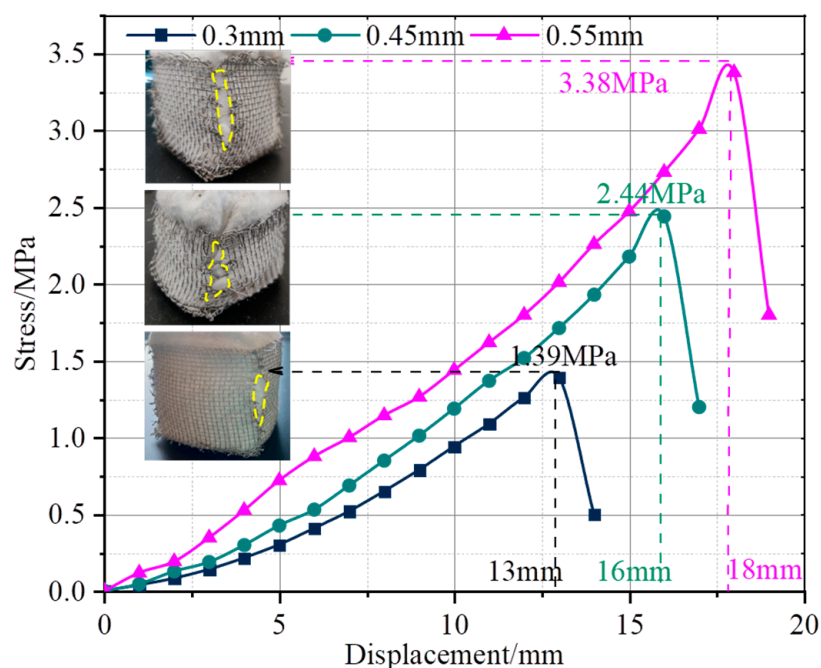


**Figure 11.** Wire diameter's impact on the mechanical properties of backfill material.

From Figure 11, it is evident that the compression stresses at the point of failure for metal mesh boxes with wire diameters of 0.3 mm, 0.45 mm, and 0.55 mm were 1.39 MPa, 2.44 MPa, and 3.38 MPa, respectively, with corresponding vertical displacements of 13 mm, 16 mm, and 18 mm. Notably, failure in all cases occurred at the edge connections of the mesh boxes. Furthermore, it is apparent that the compression stress at which the metal mesh box with a wire diameter of 0.55 mm failed was 1.39 times that of the 0.3 mm wire diameter box and 2.43 times that of the 0.45 mm wire diameter box. This suggests that filling material with thicker wire diameters exhibits a higher load-bearing capacity.

### 3.1.3. The Impact of Wire Dimensions on the Load-Bearing Performance of Backfill Material

To investigate the influence of different box dimensions on the load-bearing characteristics of wind-blown sand-filled-box-type backfill, this study selected dimensions of 5 cm, 10 cm, and 15 cm in uniaxial compression test setups, with a mesh count of 10 and wire diameter of 0.3 mm. The analysis was conducted on the test data, resulting in vertical curves as depicted in Figure 12.

From Figure 12, it is evident that the compression stresses at the point of failure for metal mesh boxes with dimensions of 5 cm, 10 cm, and 15 cm were 1.39 MPa, 0.33 MPa, and 0.18 MPa, respectively, with corresponding vertical displacements of 13 mm, 11 mm, and 9 mm. Notably, failure in all cases occurred at the edge connections of the mesh boxes. The 5 cm-sized box exhibited a more pronounced upward curvature in the curve compared to the other two, indicating that wind-blown sand-filled box-type backfill with smaller dimensions experienced a faster increase in load-bearing capacity per unit deformation. Thus, the mechanical characteristics of the smaller-sized box were superior, mainly reflected

in higher compression stress at failure, a greater maximum allowable deformation of the backfill material, and a faster growth in load-bearing capacity per unit deformation.

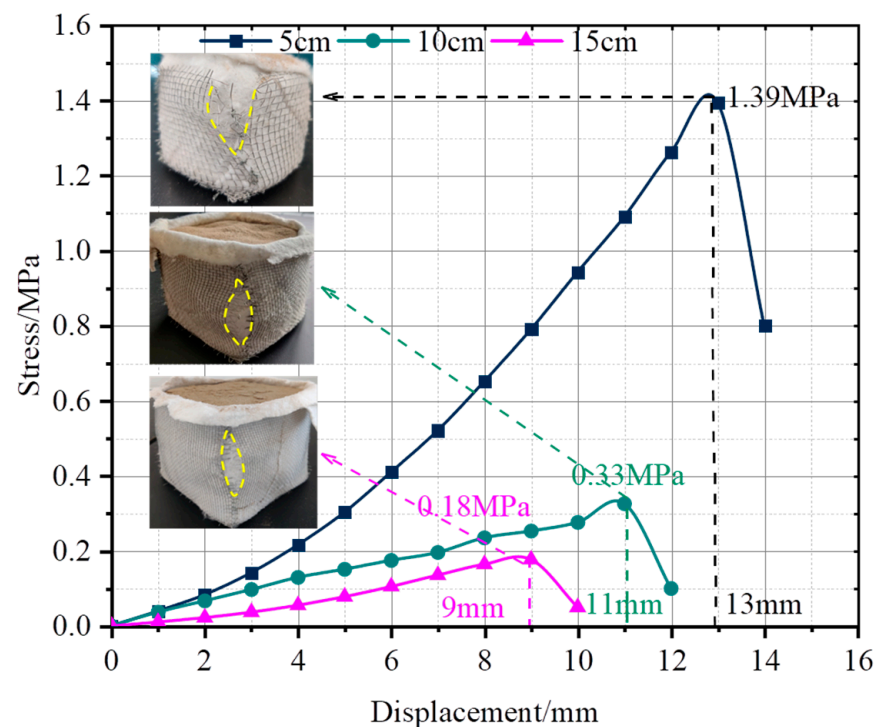


**Figure 12.** The impact of dimensions on the mechanical properties of backfill material.

### 3.2. Mechanical Performance Testing of Aeolian Sand-Box-Type Backfill

#### 3.2.1. Mechanical Performance Testing of Aeolian Sand-Box-Type Backfill

From Figure 13, it can be observed that the abscissa represents displacement and the ordinate represents stress. The curves of aeolian sand-box backfill structures with three different sizes all exhibit an upward concave growth pattern. When reaching the peak, they demonstrate brittle failure characteristics, consistent with the typical distribution of classical plastic materials [29–31]. Therefore, the mechanical properties of the aeolian sand-box backfill structure exhibit plasticity. The failure stress magnitude of the mesh boxes decreases with an increase in size. For example, the failure stress of the aeolian sand-filled mesh box with a side length of 500 mm is 0.39 MPa, while the aeolian sand-box-type backfill with a side length of 1000 mm has a significantly lower failure stress of only 0.13 MPa. In all three sizes of aeolian sand-box-type backfill, fractures occurred at the boundary connections upon reaching the failure stress, leading to the loss of load-bearing capacity for the backfill material. This is attributed to the primary lateral confinement provided by the metal wires in the aeolian sand-box-type backfill. As lateral deformation increases, both radial and transverse wires deform under external forces, generating axial forces. The combined effect of these axial forces constitutes the lateral confinement supplied by the metal mesh for the aeolian sand. Since the central part of the metal wires and the connection points experience nearly equal stress, and considering that the strength of the connection points is typically about one-third of the tensile strength of the metal wires, the boundary connections emerge as the weak points in the aeolian sand-box-type backfill.

In conclusion, when applying aeolian sand-box-type backfill in mining areas, it is essential to select the appropriate dimensions of the backfill based on the specific engineering conditions. Additionally, reinforcing the boundaries of the mesh boxes according to the intended engineering use is crucial to maximize their load-bearing performance.

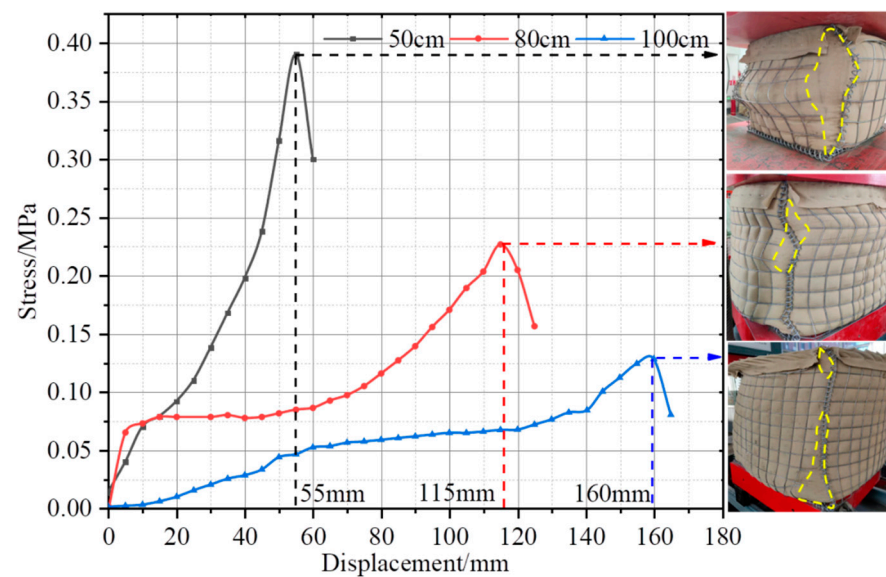


**Figure 13.** Curves of aeolian sand box-type backfill.

### 3.2.2. Numerical Simulation of Uniaxial Compression Tests on Aeolian Sand Box-Type Backfill

By utilizing a ‘trial-and-error’ method to adjust the physical mechanical parameters (friction angle, tensile strength) of different-sized aeolian sand-box backfill structures in 3DEC, the numerical simulation parameters for the backfill material are presented in Table 5. Finally, the curves obtained from the numerical simulation software were compared with those from the physical experiments, as illustrated in Figure 14.

**Table 5.** Parameters of the aeolian sand-box backfill material model [32].

Size/cm	Bulk Modulus (MPa)	Shear Strength (MPa)	Tensile Strength (MPa)	Friction Angle (°)	Density (kg/m <sup>3</sup> )
50	2.96	1.36	2.1	35	2680
80	1.33	0.62	1.7	31	2680
100	0.68	0.31	1.23	28	2680

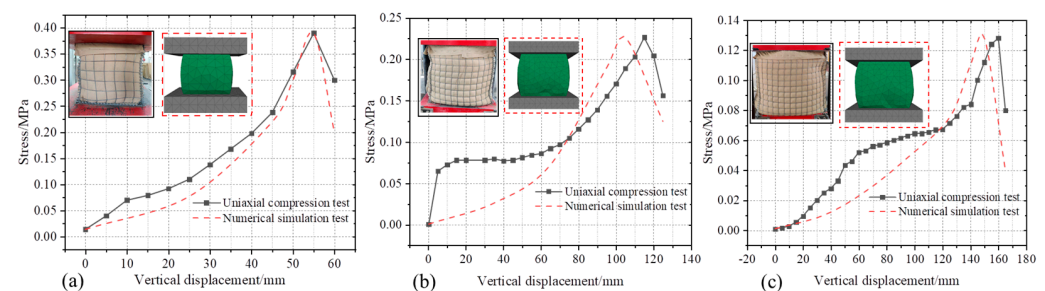


**Figure 14.** Curves of backfill material from numerical simulation and physical experiments. (a) backfill size 50 cm; (b) backfill size 80 cm; (c) backfill size 100 cm.

From (Figure 14a–c), it is evident that both the curves obtained from numerical simulations and physical experiments exhibit an initial increase followed by a decrease. The curves, in both cases, demonstrate concave upward growth before the mesh box’s failure. This behavior is attributed to the fact that the aeolian sand-box-type backfill behaves as a plastic material, and before failure, it goes through a compaction phase.

As the vertical load applied to the backfill material increases, the vertical bearing capacity of the backfill material reaches its peak and then exhibits unloading. In physical

experiments, this is manifested by the failure at the boundaries of the mesh box, leading to a loss of load-bearing capacity. In numerical simulations, it is characterized by joint sliding and fracture, resulting in a loss of load-bearing capacity. The peak strength and brittle failure obtained from both uniaxial methods are essentially consistent.

In conclusion, this section's numerical simulation method and mechanical parameter settings can support numerical simulations for backfill mining.

### 3.3. Numerical Simulation of Coal Seam Mining

#### 3.3.1. Movement Patterns of Overlying Strata during Caving Method Mining

This section examines the impact of caving method mining on overlying strata movement through the analysis of 3DEC numerical simulations. Overlying strata displacement cloud maps were generated for varying face advancement lengths (50 m, 100 m, 150 m, 200 m), illustrated in Figure 15. Vertical displacement curves for different face advancement lengths in caving method mining were created to better understand their influence on roof strata displacement, as shown in Figure 16a. Additionally, to explore the impact of both caving method and backfill mining on roof displacement, maximum roof displacement curves were generated for different face advancement lengths under both methods, as presented in Figure 16b.

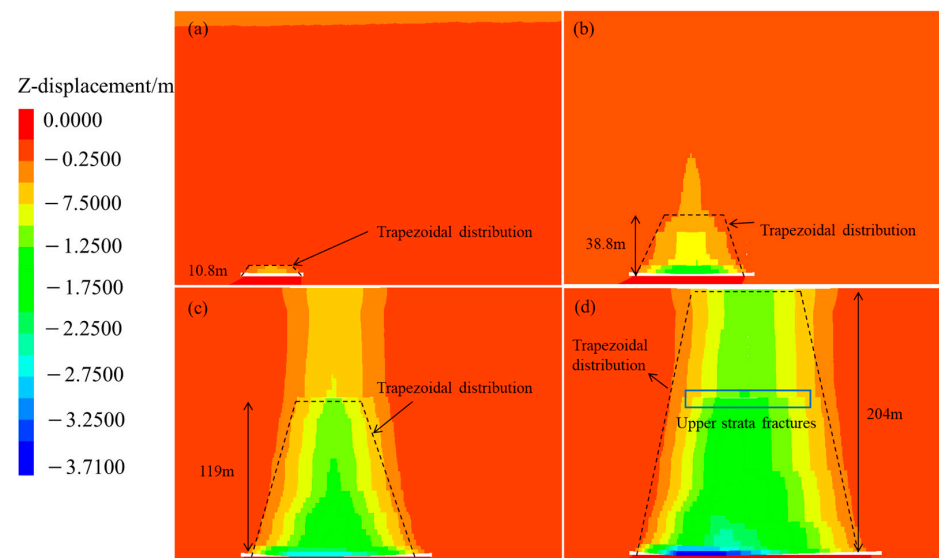


**Figure 15.** Displacement cloud map of overlying strata during caving method mining. (a) advancing 50 m; (b) advancing 100 m; (c) advancing 150 m; (d) advancing 200 m.

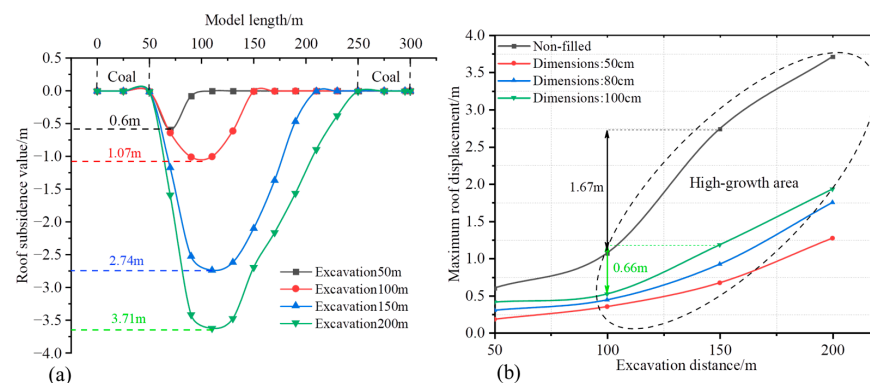


**Figure 16.** Overlying strata displacement curves during caving method mining: (a) overlying strata displacement curve for caving method mining; (b) maximum roof displacement curve at different excavation distances.

As shown in Figure 15, during coal seam mining using the caving method, the displacement of the overlying rock layers above the coal seam primarily exhibits a trapezoidal distribution, which is in line with the typical pattern of overlying strata displacement. This observation aligns with the findings of other researchers [33–35]. The collapse of the overlying strata above the coal seam intensifies with the progression of the working face. At an advancement distance of 50 m, the overlying strata experience minimal impact from coal seam mining, with the influence of coal excavation on the overlying rock layers above the coal seam reaching approximately 10.8 m in height. With an increase in coal seam advancement distance to 100 m, 150 m, and 200 m, a notable escalation in the extent of overlying strata collapse is observed. Simultaneously, the impact height of the collapse on the rock layers above the goaf also rises with the advancement distance. At advancement distances of 100 m, 150 m, and 200 m, the impact heights on the overlying rock layers measure approximately 38.8 m, 119 m, and 204 m, respectively. Examination of displacement cloud maps reveals that at an advancement distance of 150 m, there is discernible surface impact, and with a coal mining advancement distance of 200 m, surface displacement further increases.

To analyze the impact of caving and backfill mining methods on overlying strata displacement, displacement curves for overlying strata during caving method mining at different face advancement distances were generated. Maximum overlying strata displacement curves for both caving and backfill mining at various face advancement distances were also produced, corresponding to Figure 16a,b.

As shown in Figure 16a, with an increase in coal mining advancement distance, the displacement of overlying strata gradually increases. When the advancement distance is 50 m, the maximum overlying strata collapse displacement is 0.6 m. When the advancement distance is 100 m, 150 m, and 200 m, the maximum collapse displacements of the overlying strata are 1.07 m, 2.74 m, and 3.71 m, respectively. With the increase in coal mining advancement distance, the disturbed area of overlying strata also expands, and the range of overlying strata collapse increases. This phenomenon can have a detrimental impact on the surface ecological environment [36,37]. To mitigate this, it is necessary to implement backfilling in the goaf area to reduce the disturbance to the overlying strata.

As depicted in Figure 16b, a comparative analysis of maximum overlying strata displacement curves was conducted between caving method mining and backfill mining employing different sizes of backfill material. The figure clearly illustrates that backfill mining effectively mitigates the disturbance caused by coal seam excavation to the overlying strata. When utilizing aeolian sand backfill material of three different sizes in the goaf area, the maximum displacement of the overlying strata is significantly smaller compared to the caving method. For instance, at a coal seam advancement distance of 200 m, the maximum overlying strata displacement with the caving method is 3.71 m, whereas when filling the goaf area with backfill materials of 50 cm, 80 cm, and 100 cm in size, the maximum overlying strata displacements are 1.9 m, 1.7 m, and 1.2 m, respectively. Beyond an advancement distance of 100 m, both caving and backfill mining exhibit regions of elevated roof displacement. For instance, with the caving method at a 150 m advancement distance, the overlying strata displacement is 1.67 m greater than at a 100 m advancement distance. In contrast, utilizing a 100 cm-sized aeolian sand-box-type backfill material for goaf filling results in an increase of 0.66 m in overlying strata displacement when the advancement distance is 150 m compared to 100 m. Therefore, the use of aeolian sand-box-type backfill material in this study proves effective in reducing disturbance to the overlying strata to a certain extent.

### 3.3.2. Effect of Aeolian Sand-Box-Type Backfill on Overlying Strata Displacement Control

From the preceding discussion, it is evident that employing aeolian sand-box-type backfill in goaf areas can mitigate the disturbance caused by coal seam mining to the overlying strata. To assess the suitability of aeolian sand-box-type backfill for filling mining under different coal seam conditions, this section examines the control effect of various

sizes of aeolian sand-box-type backfill on the overlying strata. Curves illustrating the control effect of different backfill material sizes on overlying strata under various face advancement distances have been generated, as depicted in Figure 17.

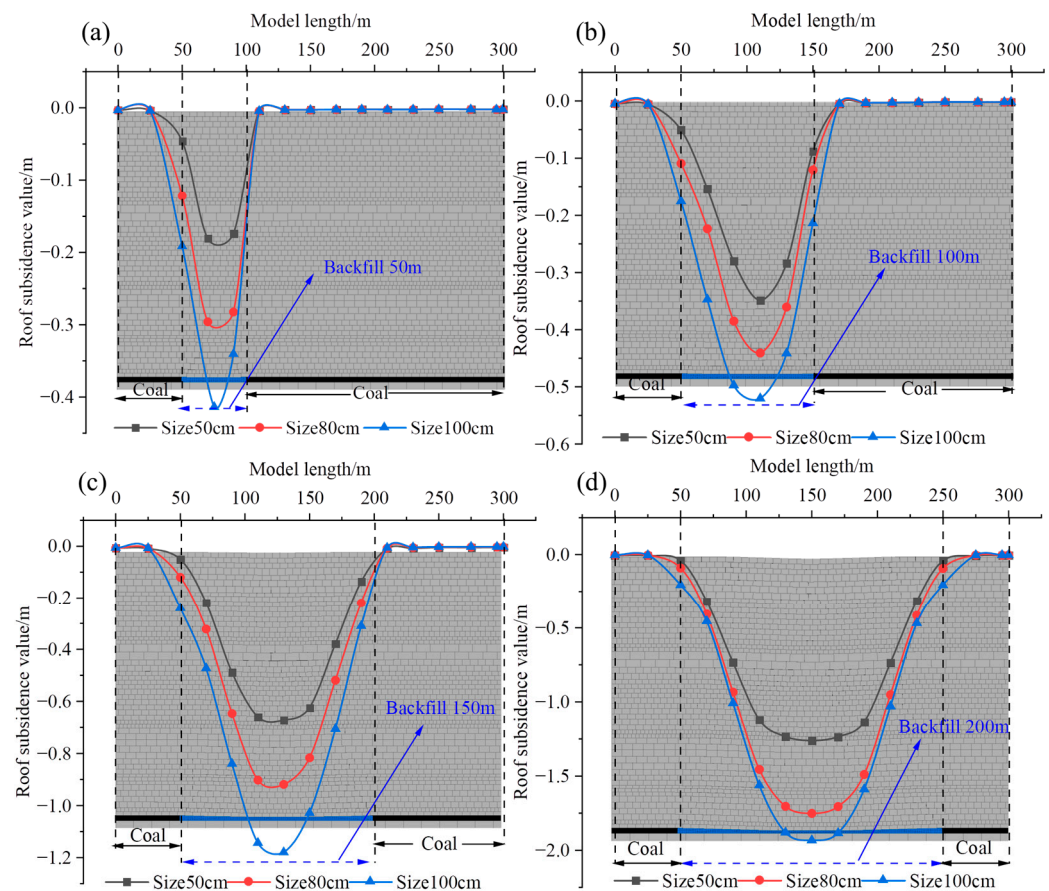


**Figure 17.** Control effect of aeolian sand-box-type backfill on overlying strata: (a) advancing 50 m; (b) advancing 100 m; (c) advancing 150 m; (d) advancing 200 m.

Observed in Figure 17a–d, the collapse curves of the overlying strata exhibit an upward concave shape when filling the goaf area at various face advancement distances with aeolian sand-box-type backfill materials of different sizes. Notably, smaller sizes of aeolian sand-box-type backfill materials demonstrate superior control over overlying strata settlement. Taking Figure 17d as an example, when filling the goaf area with aeolian sand-box-type backfill materials with side lengths of 50 cm, 80 cm, and 100 cm over a distance of 200 m, the maximum roof displacements are 1.26 m, 1.75 m, and 1.93 m, respectively. The load-bearing capacity of aeolian sand-box-type backfill materials is influenced by their size, wire diameter, and mesh size, as discussed in Section 2.2. It is known that the load-bearing capacity decreases as the size of aeolian sand-box-type backfill materials increases. In essence, smaller-sized backfill materials offer greater support to the roof, exhibiting a higher load-bearing response rate, leading to earlier compaction of the overlying strata and a reduction in displacement to some extent.

### 3.3.3. Stress Distribution Patterns in Strata during Backfill Mining

In this section, Figure 18a illustrates the impact of two coal mining methods, caving and backfilling, on the stress magnitude and distribution patterns of rock and coal pillar stresses. Additionally, Figure 18b depicts stress distribution curves for various positions within the mining face during backfill mining, considering different face advancement distances. This facilitates a comprehensive analysis of the control effect of aeolian sand-box-type backfill materials of varying sizes on the variation of rock strata stress. Furthermore,

Figure 19 provides stress contour plots for rock strata with 100 cm-sized backfill material, offering a visual analysis of stress variation and distribution patterns.

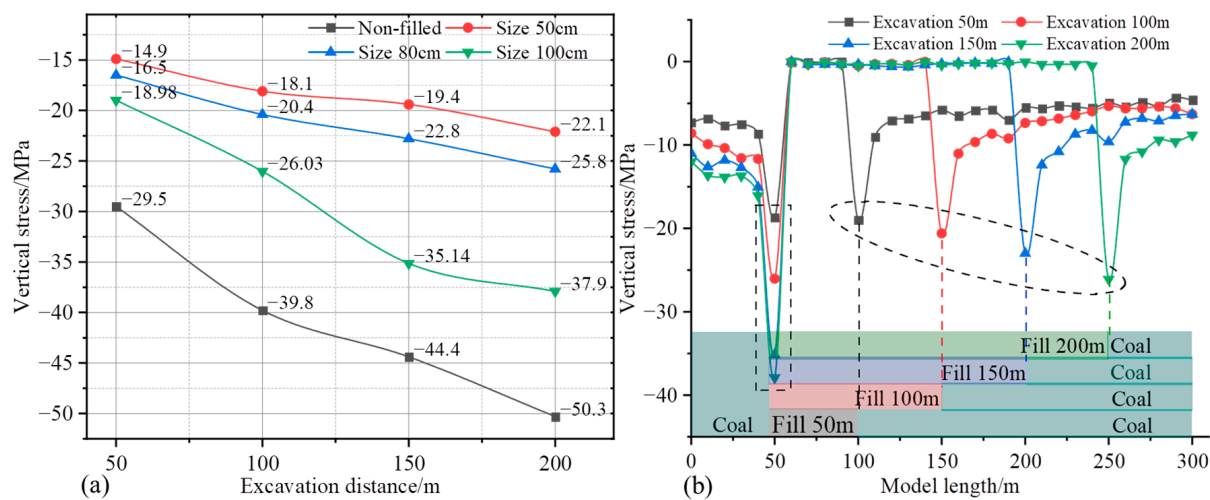


**Figure 18.** Overlying strata stress distribution curves: (a) maximum stress distribution in overlying strata; (b) relationship between rock stress and advance distance curves.

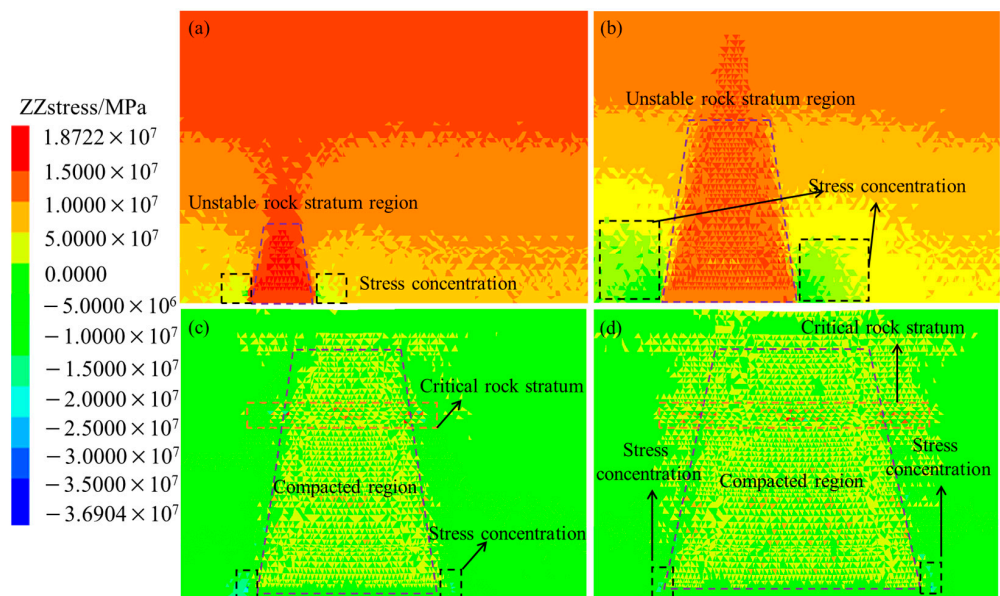


**Figure 19.** Rock stress contour maps: (a) advancing distance 50 m; (b) advancing distance 100 m; (c) advancing distance 150 m; (d) advancing distance 200 m.

From Figure 18a, it is evident that backfilling the goaf with aeolian sand-box-type backfill material effectively controls the increase in rock strata stress. At face advancement distances of 50 m, 100 m, 150 m, and 200 m, the maximum rock strata stress obtained by caving is higher than that obtained by backfill mining. For example, in the case of caving mining at a face advancement distance of 200 m, the maximum rock strata stress is  $-50.3$  MPa, while backfill mining results in a maximum rock strata stress of  $-37.9$  MPa. The maximum rock strata stress increases with the size of the backfill material. At face advancement distances of 200 m using aeolian sand-box-type backfill material with side lengths of 50 cm, 80 cm, and 100 cm, the maximum rock strata stress obtained is  $-22.1$  MPa,  $-25.8$  MPa, and  $-37.9$  MPa, respectively. Therefore, smaller-sized aeolian sand-box-type backfill material exhibits a more effective control over rock strata stress compared to larger-sized material.

To analyze the variation of maximum rock strata stress with face advancement distance during backfill mining, stress distribution curves were generated for rock strata with a 100 cm-sized aeolian sand-box-type backfill material in the goaf (Figure 18b). Observing Figure 18b, it is evident that at different face advancement distances, the maximum stress in the overlying rock strata consistently occurs just above the coal pillar. Furthermore, this maximum stress increases with the face advancement distance. For the left coal pillar, at face advancement distances of 50 m, 100 m, 150 m, and 200 m, the maximum stress above the coal pillar is  $-18.98$  MPa,  $-26.03$  MPa,  $-35.14$  MPa, and  $-37.9$  MPa, respectively. The vertical stress above the backfill material gradually increases with the face advancement distance, displaying an overall gentle and steady distribution trend [38–40].

From Figure 19, it is evident that as the advance distance increases, the disturbance range around the coal seam expands, accompanied by a notable stress concentration phenomenon near the coal pillar. Based on the aforementioned analysis, to effectively enhance the safety of coal mining operations employing aeolian sand-box-type backfilling, it is advisable to design different sizes of aeolian sand-box-type backfilling structures tailored to various coal seam conditions. This approach can help prevent the occurrence of excessive stress concentration in the coal pillar region. Examining the cloud maps reveals that at advancement distances of 50 m and 100 m, the upper rock layers above the backfilling area exhibit higher tensile stresses, gradually extending the affected area upwards. This behavior stems from the flexible nature of aeolian sand-box-type backfilling material, with its vertical load-bearing capacity increasing alongside vertical deformation. In cases where the roof subsidence is relatively small, an immediate significant vertical force may not be provided. Conversely, at advancement distances of 150 m and 200 m, the upper rock layers above the backfilling area transition from tensile stress to compressive stress. This is because with the increase in roof subsidence, the aeolian sand-box-type backfilling material provides sufficient vertical load-bearing capacity for the roof, gradually compacting the upper rock layers above the backfilling area. At this point, the overlying rock layers gradually subside with the increasing advancing distance. The key layers are primarily under compressive stress, indicating that these key layers are not prone to fracture risks and will not generate impacts affecting the underground coal mining operations' safety. In conclusion, the aeolian sand-box-type backfilling material effectively controls rock layer displacement and stress distribution.

#### 4. Conclusions

This paper investigates the influence of filament diameter, pore size, and dimensions on the bearing performance of aeolian sand-filled box-type fill materials through uniaxial compression tests and mechanical analysis. The mechanical equation for the net box constraint force in relation to the iron wire's filament diameter, pore size, and dimensions is derived. The study employs numerical simulation to analyze the control effect of aeolian sand-filled box-type fill materials on overlying strata. The key findings are as follows:

1. Uniaxial compression tests on the aeolian sand-filled box-type fill material model reveal that the bearing capacity of the filling material increased with the augmentation of wire diameter and mesh density. Conversely, the bearing capacity of the aeolian sand-filled box decreased with the enlargement of dimensions. The compression stress at the failure of metal mesh boxes with dimensions of 5 cm, 10 cm, and 15 cm were 1.39 MPa, 0.33 MPa, and 0.18 MPa, respectively.
2. Force analysis was conducted on the metal mesh box on the outer side of the aeolian sand-filled box-type filling. The mechanical relationship equation between the lateral restraining force provided by the mesh box for the aeolian sand during the bearing deformation and the wire diameter, mesh size, and dimensions was derived. Additionally, the force-deformation equation at the boundary connection of the mesh box was obtained.
3. Physical uniaxial compression tests and numerical simulations were performed on aeolian sand-filled box-type fill materials in three different sizes (50 cm, 80 cm, 100 cm).

Both methods produced curves characterized by an initial increase followed by a decrease. The curves from the two approaches closely matched, indicating good agreement. Mechanical parameters derived from numerical simulations were found to be reasonably accurate.

4. A comparative analysis was conducted on the maximum vertical displacement of overlying strata obtained through the caving method and backfill mining method. It was observed that the aeolian sand-filled box-type filling structure can effectively control overlying strata displacement. Moreover, smaller dimensions of the aeolian sand-filled box-type filling structure resulted in a more pronounced control effect on overlying strata movement.
5. The aeolian sand-filled box-type filling structure effectively alleviates high stress concentration issues in the coal pillar and overlying rock strata post-coal seam extraction. Under the caving method, the maximum stress in the rock strata at an advancing distance of 200 m reached  $-50.3$  MPa, compared to  $-37.9$  MPa with the backfill mining method. The maximum stress in the rock strata correlates positively with the enlargement of the filling structure size.

**Author Contributions:** Conceptualization, B.Z., X.G. and S.F.; methodology, B.Z.; software, B.Z., W.W. and D.Y.; validation, B.Z.; formal analysis, W.W., H.C., W.G., X.L., D.Y., L.H. and Y.Z.; investigation, W.W.; resources, Z.Z., W.G. and X.L.; data curation, W.W.; writing—original draft preparation, B.Z.; writing—review and editing, B.Z.; visualization, Z.Z., X.G. and S.F.; supervision, W.W. and X.T.; project administration, B.Z.; funding acquisition, X.T., L.H., Y.Z. and H.C. All authors have read and agreed to the published version of the manuscript.

**Funding:** This project is supported by the National Natural Science Foundation of China (Regional Project No. 51964042), the Natural Science Youth Project of the Autonomous Region's University Research Plan (XJEDU2018Y013), the Tianshan Youth Program for Young Doctoral Scientific and Technological Talent Cultivation in Xinjiang Uygur Autonomous Region (Project No. 2019Q063), and the Xinjiang Uygur Autonomous Region Major Science and Technology Special Project (2022A03015).

**Data Availability Statement:** Data are contained within the article.

**Acknowledgments:** We acknowledge the administrators and technicians in the Xinjiang Wucaiwan coal field for their contributions to the aeolian sand collection and geological data provision. We also thank the editors and reviewers for their comments on this paper.

**Conflicts of Interest:** The authors declare no conflict of interest.

## References

1. Bi, X.; Chang, B.; Hou, F.; Yang, Z.; Fu, Q.; Li, B. Assessment of Spatio-Temporal Variation and Driving Mechanism of Ecological Environment Quality in the Arid Regions of Central Asia, Xinjiang. *Int. J. Environ. Res. Public Health* **2021**, *18*, 7111. [\[CrossRef\]](#) [\[PubMed\]](#)
2. Zhang, J.; Zhang, M.; Yu, J.; Yu, Y.; Yu, R. Comparison of Flash Drought and Traditional Drought on Characteristics and Driving Forces in Xinjiang. *Remote Sens.* **2023**, *15*, 4758. [\[CrossRef\]](#)
3. Fan, T.; Pan, J.; Wang, X.; Wang, S.; Lu, A. Ecological Risk Assessment and Source Apportionment of Heavy Metals in the Soil of an Opencast Mine in Xinjiang. *Int. J. Environ. Res. Public Health* **2022**, *19*, 15522. [\[CrossRef\]](#) [\[PubMed\]](#)
4. Aizizi, Y.; Kasimu, A.; Liang, H.; Zhang, X.; Wei, B.; Zhao, Y.; Ainiwaer, M. Evaluation of Ecological Quality Status and Changing Trend in Arid Land Based on the Remote Sensing Ecological Index: A Case Study in Xinjiang, China. *Forests* **2023**, *14*, 1830. [\[CrossRef\]](#)
5. Wu, J.; Xie, D.; Yi, S.; Yin, S.; Hu, D.; Li, Y.; Wang, Y. Fractal Study of the Development Law of Mining Cracks. *Fractal Fract.* **2023**, *7*, 696. [\[CrossRef\]](#)
6. Tang, Y.; Wang, Z.; Sun, W.; Wang, W.; Yang, H. Research Development and Critical Problems Existing in Strata Movement and Its Control. *Energies* **2023**, *16*, 6065. [\[CrossRef\]](#)
7. Marian, D.P.; Onica, I. Analysis of the Geomechanical Phenomena That Led to the Appearance of Sinkholes at the Lupeni Mine, Romania, in the Conditions of Thick Coal Seams Mining with Longwall Top Coal Caving. *Sustainability* **2021**, *13*, 6449. [\[CrossRef\]](#)
8. Thakur, T.K.; Dutta, J.; Bijalwan, A.; Swamy, S.L. Evaluation of decadal land degradation dynamics in old coal mine areas of Central India. *Land Degrad. Dev.* **2022**, *33*, 3209–3230. [\[CrossRef\]](#)

9. Popczyk, M.K.; Jendrus, R. Impact of ash and water mixture density on the process of gob grouting in view of laboratory tests. *Arch. Min. Sci.* **2019**, *64*, 625–634.
10. Eldridge, D.J.; Oliver, I.; Powell, J.R.; Dorrough, J.; Carrillo, Y.; Nielsen, U.N.; Macdonald, C.A.; Wilson, B.; Fyfe, C.; Amarasinghe, A.; et al. Temporal dynamics in biotic and functional recovery following mining. *J. Appl. Ecol.* **2022**, *59*, 1632–1643. [\[CrossRef\]](#)
11. Shi, X.; Yang, Y.; Ding, H.; Chen, F.; Shi, M. Analysis of the Variability Characteristics and Applicability of SPEI in Mainland China from 1985 to 2018. *Atmosphere* **2023**, *14*, 790. [\[CrossRef\]](#)
12. Li, X.; Zulkar, H.; Wang, D.; Zhao, T.; Xu, W. Changes in Vegetation Coverage and Migration Characteristics of Center of Gravity in the Arid Desert Region of Northwest China in 30 Recent Years. *Land* **2022**, *11*, 1688. [\[CrossRef\]](#)
13. Zhou, Y.; Gao, X.; Lei, J. Characteristics of Dust Weather in the Tarim Basin from 1989 to 2021 and Its Impact on the Atmospheric Environment. *Remote Sens.* **2023**, *15*, 1804. [\[CrossRef\]](#)
14. Song, C.; Teni, G.; Du, H. Spatio-Temporal Evolution of Ecological Sensitivity in the Desert of China from 1981 to 2022. *Sustainability* **2023**, *15*, 12102. [\[CrossRef\]](#)
15. Amin, M.N.; Iqbal, M.; Ashfaq, M.; Salami, B.A.; Khan, K.; Faraz, M.I.; Alabdullah, A.A.; Jalal, F.E. Prediction of Strength and CBR Characteristics of Chemically Stabilized Coal Gangue: ANN and Random Forest Tree Approach. *Materials* **2022**, *15*, 4330. [\[CrossRef\]](#) [\[PubMed\]](#)
16. Gu, W.; Chen, L.; Xu, D. Research on the Overburden Movement Law of Thick Coal Seam Without-Support Gangue-Filling Mining. *Minerals* **2023**, *13*, 53. [\[CrossRef\]](#)
17. Ashfaq, M.; Moghal, A.A.B.; Basha, B.M. The Sustainable Utilization of Coal Gangue in Geotechnical and Geoenvironmental Applications. *J. Hazard. Toxic Radioact. Waste* **2022**, *26*, 3122003. [\[CrossRef\]](#)
18. Farshadi, A.; Mehrnahad, H.; Abdoli, M. Effects of glass fibers and nanoclay on the strength parameters of aeolian sand: An experimental study. *Bull. Eng. Geol. Environ.* **2023**, *82*, 278. [\[CrossRef\]](#)
19. Maksimov, F.; Tombari, A. Derivation of Cyclic Stiffness and Strength Degradation Curves of Sands through Discrete Element Modelling. *Modelling* **2022**, *3*, 400–416. [\[CrossRef\]](#)
20. Huang, P.; Zhang, J.; Yan, X.; Spearing, A.J.S.; Li, M.; Liu, S. Deformation response of roof in solid backfilling coal mining based on viscoelastic properties of waste gangue. *Int. J. Min. Sci. Technol.* **2021**, *31*, 279–289. [\[CrossRef\]](#)
21. Zhang, Z.; Wang, W.; Zhao, B. Numerical Study on the Vibratory Compaction Mechanism of the Sand-Gabion Backfills in Underground Coal Mines. *Minerals* **2022**, *12*, 1428. [\[CrossRef\]](#)
22. Zhang, Z.; Liu, H.; Su, H.; Zeng, Q. Green Mining Takes Place at the Power Plant. *Minerals* **2022**, *12*, 839. [\[CrossRef\]](#)
23. Du, W.; Nie, R.; Tan, Y.; Zhang, J.; Qi, Y.; Zhao, C. Influence of Strengthened Nodes on the Mechanical Performance of Aeolian Sand—Geogrid Interface. *Materials* **2023**, *16*, 4665. [\[PubMed\]](#)
24. Ren, Z.; Pan, J.; Li, Z.; Xiao, P.; Shen, Z.; Jia, L.; Li, X. The Interaction of Aeolian Sand and Slope on Runoff and Soil Loss on a Loess Slope via Simulated Rainfall under Laboratory Conditions. *Water* **2023**, *15*, 888. [\[CrossRef\]](#)
25. Arias-Trujillo, J.; Matías-Sánchez, A.; Cantero, B.; López-Querol, S. Effect of polymer emulsion on the bearing capacity of aeolian sand under extreme confinement conditions. *Constr. Build. Mater.* **2020**, *236*, 117473. [\[CrossRef\]](#)
26. Frid, V.; Potirakis, S.M.; Shulov, S. Study of Static and Dynamic Properties of Sand under Low Stress Compression. *Appl. Sci.* **2021**, *11*, 3311. [\[CrossRef\]](#)
27. Yan, S.; Zhang, S.; Chen, W.; Zhao, Y. Analysis of Mechanical Stress on Metal Mesh. *China Energy Environ. Prot.* **1987**, *3*, 7–12.
28. Sun, Z.; Lin, J. Theoretical Analysis on Mechanical Performance of Bolt Metal Meshes. *Coal Technol.* **2014**, *33*, 98–100.
29. Khatami, H.; Deng, A.; Jaksa, M. Passive arching in rubberized sand backfills. *Can. Geotech. J.* **2019**, *57*, 549–567. [\[CrossRef\]](#)
30. Zhang, C.; Liu, G.; Tian, S.; Cai, M. Passive Soil Arching Effect in Aeolian Sand Backfills for Grillage Foundation. *Sensors* **2023**, *23*, 8098. [\[CrossRef\]](#)
31. Khatami, H.; Deng, A.; Jaksa, M. The arching effect in rubber–sand mixtures. *Geosynth. Int.* **2020**, *27*, 432–450. [\[CrossRef\]](#)
32. Li, L.; Zheng, Z.; Yan, H.; Huang, S.; Zhou, X. Analysis of Earth Pressure on Reinforced Soil Retaining Wall with Geogrid Reinforcement and Improvement of Calculation Methods. *J. Northwest. Polytech. Univ.* **2022**, *40*, 1366–1374. [\[CrossRef\]](#)
33. Han, Y.; Wei, C.; Cui, M.; Xie, H.; Ou, Y.; Zhu, H.; Liu, T. Ground Settlement of Deeply Buried Two-Lane Tunnels with Large Cross-Sections Using Different Construction Methods. *Appl. Sci.* **2022**, *12*, 11105. [\[CrossRef\]](#)
34. Dong, Y.; Luan, Y.; Ji, Z.; Luan, H. Optimization of Physical Parameters and Analysis of Rock Movement and Deformation Patterns in Deep Strip Mining. *Appl. Sci.* **2023**, *13*, 506. [\[CrossRef\]](#)
35. Jiang, N.; Lv, K.; Gao, Z.; Di, H.; Ma, J.; Pan, T. Study on Characteristics of Overburden Strata Structure above Abandoned Gob of Shallow Seams—A Case Study. *Energies* **2022**, *15*, 9359. [\[CrossRef\]](#)
36. Raffaldi, M.J.; Seymour, J.B.; Richardson, J.; Zahl, E.; Board, M. Cemented Paste Backfill Geomechanics at a Narrow-Vein Underhand Cut-and-Fill Mine. *Rock Mech. Rock Eng.* **2019**, *52*, 4925–4940. [\[CrossRef\]](#) [\[PubMed\]](#)
37. Gabarron, M.; Zornoza, R.; Acosta, J.A.; Faz, A.; Martínez-Martínez, S. Mining environments. *Adv. Chem. Pollut. Environ. Manag. Prot.* **2019**, *4*, 157–205.
38. Saghafi, A.; Pinetown, K.L. A new method to determine the depth of the de-stressed gas-emitting zone in the underburden of a longwall coal mine. *Int. J. Coal Geol.* **2015**, *152*, 156–164. [\[CrossRef\]](#)

39. Mirenkov, V.E. Influence of Stresses and Displacements in Roof Rocks on Roof Fracture in Top Coal Caving. *J. Min. Sci.* **2020**, *56*, 203–208. [[CrossRef](#)]
40. Greb, S.F.; Nelson, W.J.; Elrick, S.D. Mining geology of the principal resource coals of the Illinois Basin. *Int. J. Coal Geol.* **2020**, *232*, 103589. [[CrossRef](#)]

**Disclaimer/Publisher’s Note:** The statements, opinions and data contained in all publications are solely those of the individual author(s) and contributor(s) and not of MDPI and/or the editor(s). MDPI and/or the editor(s) disclaim responsibility for any injury to people or property resulting from any ideas, methods, instructions or products referred to in the content.